

Texture Effect on Fatigue Crack Propagation Behavior in Annealed Sheets of an Al-Cu-Mg Alloy

Peng Xia, Zhiyi Liu, Wenting Wu, Qi Zhao, Puyou Ying, and Song Bai

(Submitted February 27, 2018; in revised form July 4, 2018; published online August 20, 2018)

The effects of texture, including Brass, Goss + Cube and Cube, on the fatigue crack growth behavior in annealed Al-Cu-Mg alloy sheets were characterized in this investigation. Results showed that the Goss + Cube sheet possessed the greatest fatigue threshold value and the lowest fatigue crack propagation (FCP) rate, and the Brass sheet presented the smallest threshold value and the greatest FCP rate among the three textured sheets. SEM results showed more slip bands and more tortuous crack path formed in Goss + Cube sheet during cyclic loading, and EBSD results showed that numerous dramatic crack deflections occurred when fatigue crack propagated across Goss-grain boundary in Goss + Cube sheet, indicating that the grain orientations including Goss and Cube had positive effect on enhancing the FCP resistance. On the one hand, Goss and Cube grains have more high Schmid factor slip systems than Brass grain, promoting persistent slip bands formation and externally applied energy consumption, consequently giving rise to a high resistance to FCP. On the other hand, Goss grains could induce crack deflection with large twist angles, resulting in more energy consumption during the cracking process and thereby enhance the FCP resistance.

Keywords Al-Cu-Mg alloy, crack deflection, fatigue crack propagation, persistent slip bands, texture

1. Introduction

Many investigations focused on Al-Cu-Mg alloys due to their low density, moderate strength, high corrosion resistance and good damage tolerance (Ref 1-6). Fatigue fracture, as a fracture frequently seen in aircraft damage, attracted much attention in recent decades. It has been revealed that the fatigue crack propagation (FCP) behavior was mainly influenced by the grain size, secondary phase, grain orientation and inclusion particles (Ref 7-9). For Al-Cu-Mg alloys, solute clusters and secondary precipitate phases played an important role in the fatigue crack propagation. It was reported that the coherent Cu-Mg co-clusters promoted the reversible dislocation slipping at the fatigue crack tip, benefiting to reducing the fatigue damage accumulation and the crack closure (Ref 10, 11). Similarly, some secondary precipitates which can be cut by the dislocations such as the coherent σ' , semi-coherent θ' , Ω precipitates, also can increase the reversibility of dislocation slipping and finally reducing fatigue damage accumulation (Ref 12-14). Besides solute clusters and secondary phases, the grain orientation was considered to have significant impact on FCP (Ref 15-19). Zhai (Ref 15) revealed that the deflection of short fatigue crack at the grain boundary was decided by the orientation relation between the two favorable slip planes of the neighboring grains. This orientation relation can be character-

ized by the twist angle α and the tilt angle β , which were determined by the crystallographic orientations of the neighboring grains. It was revealed that Goss grains tended to offer large twist angles to their neighboring grains, promoting crack deflection with large crack twist angles at their grain boundary (Ref 16, 18). This crack propagation with more twisting deflection consumed more energy during cracking process, in favor of reducing the FCP rate (Ref 15-18).

Previous investigations (Ref 17-19) about the effect of grain orientations on FCP mainly focused on the aging tempered Al-Cu-Mg alloy, in which the majority of grains possessed the Cube or Goss orientations while only a small number of Brass grains remained after the solution treatment. Previous works (Ref 16-18) have confirmed that Goss grains offered higher FCP resistance to the fatigue crack across their grain boundaries. However, the effect of a high intensity of Cube texture on the FCP behavior was not clear. More seriously, up to now, scarcely any researches have been conducted on the effect of a high intensity Brass texture on the fatigue crack propagation behavior. This is mainly because a high intensity Brass texture is difficult to be obtained in the fully recrystallized alloy. In the recent study (Ref 20), it was revealed that the deformed Brass texture could increase to some extent at the beginning of recrystallization annealing. The result showed that the enhancement of Brass texture was attributed to the grain boundary migration occurring during the recovery process (Ref 20). In present work, an Al-Cu-Mg alloy sheet with a dominant Brass texture was obtained by means of a low-temperature annealing. Meanwhile, the sheets mainly consist of Cube or Goss textures could also be acquired through adjusting the temperature and time parameters of annealing. Previous work (Ref 17-19) mainly focused on the effect of grain orientations on the FCP behavior in Paris regime, while the crack propagation behavior in near-threshold regime influencing by the texture was not investigated. Zhao (Ref 21) has studied the effect of Goss and Brass textures on the fracture toughness of the annealed Al-Cu-Mg alloy. However, the fracture toughness is different from the

Peng Xia, Zhiyi Liu, Wenting Wu, Qi Zhao, Puyou Ying, and Song Bai, Key Laboratory of Nonferrous Metal Materials Science and Engineering, Ministry of Education, Central South University, Changsha 410083, China; and School of Material Science and Engineering, Central South University, Changsha 410083, China. Contact e-mail: liuzhiyi335@163.com.

fatigue crack resistance in essence. And the crack propagation in the fracture toughness testing shows higher FCP rates, similar to the crack propagation in Paris regime, which is different from the short crack propagation in fatigue testing. The present work aimed at exploring the effect of high intensity Brass, Goss and Cube textures on the short fatigue crack propagation behavior in near-threshold regime of annealed Al-Cu-Mg alloy sheets. The persistent slip band (PSB) as a typical characteristic of the fatigue behavior, highly depending on the grain orientation was analyzed in this work. Besides, a crystallographic model for short fatigue crack propagation was employed to calculate the twist and tilt angles of crack deflections, so as to reveal the effect of grain orientations on the fatigue crack deflection.

2. Experimental

The material used in this investigation was commercial Al-Cu-Mg aluminum alloy, and the nominal chemical composition was 4.0% Cu, 1.4% Mg, 0.6% Mn, 0.02%Ti, 0.06% Fe, 0.06% Si (in wt.%). The alloy was received in homogenized condition, hot rolled to 3 mm in thickness. Then the hot rolled sheets, named sheets A, B, and C, were subjected to 370 °C/4 h, 420 °C/2 h, and 460 °C/2 h annealing treatments, respectively, in order to obtain three annealed sheets with different texture components. By means of the x-ray diffraction (XRD) technique, the texture components of annealed sheets were measured. The (111), (200), and (220) pole figures were examined by the Schulz back-reflection method using $\text{CuK}\alpha$ radiation. The orientation distribution functions (ODFs) were calculated from the incomplete pole figures using the series expansion method ($l_{\text{max}} = 16$). Tensile testing was conducted on a CSS-44100 tension machine with 2 mm/min loading speed. Volume fractions of the measured ideal orientations were calculated by integration within 15° of the ideal orientation peaks. Optical metallographic examination was used to reveal the grain structures. The secondary phase particle size and distribution were identified through a FEI Quanta 200 scanning electron microscopy (SEM). The fine precipitates in grain interior were characterized by transmission electron microscopy (TEM) on a Tecnai G²20 TEM machine equipped with EDAX Genesis (EDS). The compact tension (CT) samples with a size of 45.6 mm × 38 mm × 3 mm (L × W × B), taken from the sheet in the L–T orientation, were electropolished in a solution

of 90% ethanol and 10% perchloric acid. All FCP tests for CT samples were performed on an MTS machine at room temperature and in air, with the loading direction paralleled to the L-direction. And a sinusoidal cyclic constant loading with a stress ratio ($R = \sigma_{\text{min}}/\sigma_{\text{max}}$) of 0.1 and a frequency of 10 Hz was applied in the FCP test. Fatigued samples were unloaded when ΔK reached 15 $\text{Mpa}\sqrt{\text{m}}$. Then fatigue surface morphology was analyzed by SEM through the FEI Quanta 200 scanning electron microscope. To detect the crack propagation paths and the grain orientation distributions along the fatigue crack, the electron back scatter diffraction (EBSD) method was employed. EBSD samples were prepared by mechanical grind, and electropolishing. All EBSD experiments were performed on a FEI Helios Nanolab 600i field emission gun scanning electron microscope with an accelerating voltage of 20 kV.

3. Results

3.1 Textures and Tensile Properties

Figure 1 shows that the representative ODF sections of annealed Al-Cu-Mg alloy sheets. The texture in sample A was mainly Brass, with the orientation intensity $f(g)$ of 24. The texture in sample B was mainly composed by Goss and Cube, whose orientation intensity $f(g)$ s reach 12 and 6, respectively. The texture in sample C was mainly Cube, with the orientation intensity $f(g)$ of 25. The texture volume fractions of various annealed Al-Cu-Mg alloy sheets are present in Table 1. The result showed that the texture in samples A, B and C was predominated by Brass, Goss + Cube and Cube, respectively. The tensile properties of the two conditions are represented in Table 2. It can be observed that sample A showed relatively higher tensile and yield strengths but a lower elongation, as compared to samples B and C.

3.2 Fatigue Crack Growth

Figure 2 illustrates the fatigue crack propagation rate curves (da/dN versus ΔK) of samples A, B and C. Sample B with a dominant Goss + Cube texture showed the lowest fatigue crack propagation rate and the highest threshold value (ΔK_{th}) among the three textured sheets. In contrast, sample A with a dominant Brass texture represented the highest FCP rate and the smallest ΔK_{th} . At the ΔK of 15 $\text{Mpa}\sqrt{\text{m}}$, the FCP rates in sample A, B and C were 4.55×10^{-4} mm/cycle, 1.30×10^{-4} mm/cycle

Table 1 Texture volume fractions (%) of Al-Cu-Mg alloy sheets

Samples	Brass	Goss	Cube	Copper	S	Random
A	45.7	4.2	5.1	13.6	4.1	27.3
B	3.6	23.7	11.4	3.2	0	52.1
C	0	5.5	51.7	0	0	42.8

Table 2 Tensile properties of Al-Cu-Mg alloy sheets

Samples	Tensile strength, Mpa	Yield strength, Mpa	Elongation, %
A	335	218	16.5
B	317	206	17.8
C	322	210	19.1

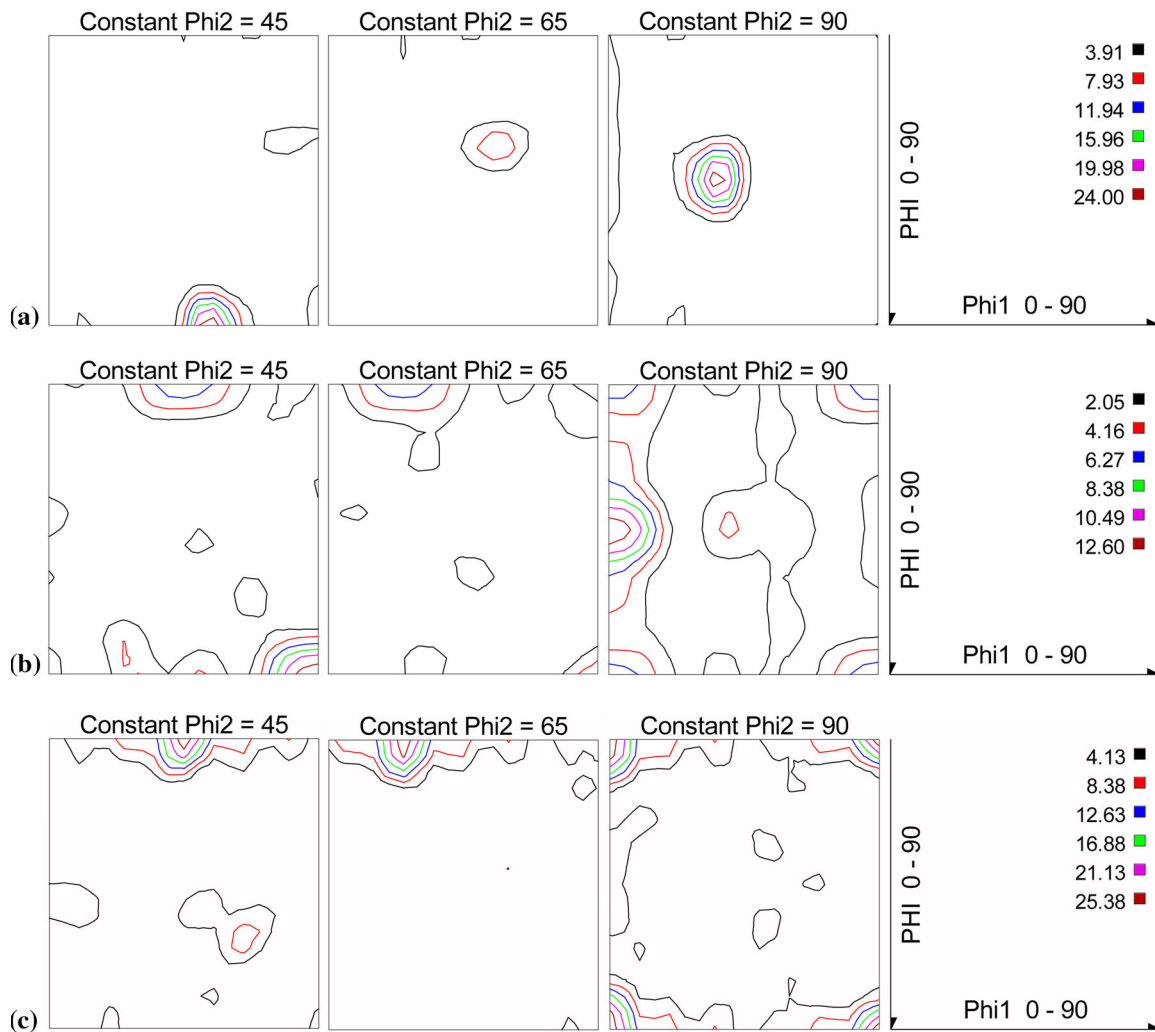


Fig. 1 Texture measurement results showing ODFs sections for sample A (a), sample B (b) and sample C (c)

and 2.64×10^{-4} mm/cycle, respectively. Apparently, the grain orientations should have significant impact on FCP, even though there might be other microstructural effects, such as grain size and inclusion particles etc., on influencing the fatigue behavior.

3.3 Microstructural Characterization

The optical micrographs of the annealed Al-Cu-Mg alloy are shown in Fig. 3. It can be observed that the microstructure of sample A mainly consisted of some elongated grains, similar to the microstructure in the rolling condition, as shown in Fig. 3(a). In contrast, some small approximately equiaxed grains of samples B and C can be clearly seen in Fig. 3(b) and (c), indicating the onset of recrystallization. Besides, the elongated grains were also found in samples B and C, but showed larger grain sizes as compared to that in sample A. These large elongated grains were probably produced by the crystal growth during the recrystallization.

The secondary particle size and distribution of the three annealed samples were characterized by SEM observation in Fig. 4. The back-scattered electron (BSE) images revealed that sample A owned the largest particle size and the highest particle density while sample C owned the smallest particle size and the lowest particle density. It is proposed that the

high temperature annealing could facilitate the dissolution of secondary particles. EDS analysis results showed that the secondary particles in three annealed samples have similar compositions, whose Cu/Mg atomic ratios were all close to 3/1.

Figure 5 represents the bright-field TEM micrographs and corresponding selected area electron diffraction (SAED) patterns of the annealed Al-Cu-Mg alloy. A large number of subgrains with the similar orientations were found in the grain interior of sample A, as shown in Fig. 5(a). It suggested that a obvious recovery occurred in sample during annealing at 370 °C. In contrast, subgrains were absent in both samples B and C, as shown in Fig. 5(b) and (c), indicating the recrystallization was completed in both samples B and C. Besides, some rod-like particles were observed in all samples and this rod-like phase was recognized as T phase ($\text{Al}_{20}\text{Cu}_2\text{Mn}_3$) (Ref 22-24). The EDS analysis of the rod-like particle shown in Fig. 5(d) confirmed that its atomic ratio (AlCuMn) was close to 20:2:3. It was reported that T phase usually formed during homogenization and kept stable during subsequent heat treatments (Ref 22, 23). As shown in Fig. 5(a), (b) and (c), the quantity of T phase particles in samples B and C was slightly larger than that in samples A, indicating the effect of annealing temperature on the precipitation of T phase is limited.

3.4 Fatigue Surface Morphology

Figure 6 shows the surface morphology near the fatigue crack tip of different samples. It can be observed that the persistent slip bands with two different directions developed in samples surface. It suggested that multiple slip systems were activated during the cyclic plastic deformation. However, the fatigue crack still propagated along the direction paralleled to slip bands. This fatigue crack propagation manner was similar to that in the Stage I of fatigue fracture which was dominated by the single slip mechanism, mentioned in Ref 25. As shown in Fig. 6, samples B and C possessed more PSBs than sample A. It was reported that PSBs could benefit the reversible cycle slip and promote the crack deflection along the favor slip system (Ref 6, 26, 27). Besides, sample A showed relatively smooth crack paths and large crack opening displacements. In contrast, more tortuous crack paths and appreciable crack closure were found in samples B and C. This high level of crack closure could significantly reduce the FCP rate. Moreover, as shown in Fig. 6(b), a distinct secondary crack was found in sample B, which was considered to be beneficial for enhancing the resistance of FCP (Ref 26, 28, 29).

3.5 Fatigue Crack Propagation Path

The short crack propagation paths in sample A, B, and C were characterized by means of EBSD, as shown in Fig. 7. Table 3 represents the orientations of grains near fatigue crack

of samples A, B and C. The crack deflections marked by numerals in Fig. 7 can be divided into two types: the crack deflection in the grain interior and the crack deflection at the grain boundary. It was observed that the orientations of grains in sample A were mainly close to Brass. Considering the orientation indices of grains C and D in were similar to each other and both close to the Brass orientation $\{011\} \langle 211 \rangle$, crack deflection 2 as shown in Fig. 7(a) can be approximately regarded as a crack deflection in the grain interior. Besides, it was observed that the crack path in grains C and D shown in Fig. 7(a) was exactly coincided with the crack path shown in Fig. 6(a). It indicated that the area involved in Fig. 6(a) was mainly occupied by the Brass grains. The orientations of grains in sample B were mainly closed to Goss or Cube. Crack deflections 1 and 2 occurred in grain A, whose grain orientation was close to Cube. Crack deflections 3 and 6 occurred in grain B and F, respectively, whose grain orientations were both close to Goss. Crack deflections 4, 5, 7 and 8 occurred at the grain boundary between the Cube and Goss or near-Goss grains. The crack path in grain F in sample B shown in Fig. 7(b) was coincided with the crack path shown in Fig. 6(b), indicating that the area involved in Fig. 6(b) was mainly occupied by the near-Goss grains. The orientations of grains in sample C were mainly closed to Cube. Deflection 1 occurred at the boundary between grain B (close to Brass) and grain C (close to Cube). Deflection 2 occurred in the interior of grain C while deflections 3 and 4 occurred at boundary between two near-Cube grains, respectively. The crack path near the crack tip shown in Fig. 7(c) was coincided with the crack path shown in Fig. 6(c), indicating that the area involved in Fig. 6(c) was mainly occupied by the Cube or near-Cube grains.

4. Discussion

4.1 The Influence of the Secondary Particles

It is well known that the fatigue crack propagation (FCP) behavior was mainly influenced by secondary particles, grain size and grain orientations (Ref 7-9). The BSE images shown in Fig. 4 revealed that the secondary particles with the largest size and the highest density were present in sample A as compared to other samples. Large secondary phases were believed to promote the nucleation of microscopic cracks during cycle deformation (Ref 23, 26, 30). Due to the local deformation inharmony between secondary particles and the matrix, the secondary particles could debond from the matrix along the direction normal to the loading direction, resulting in the

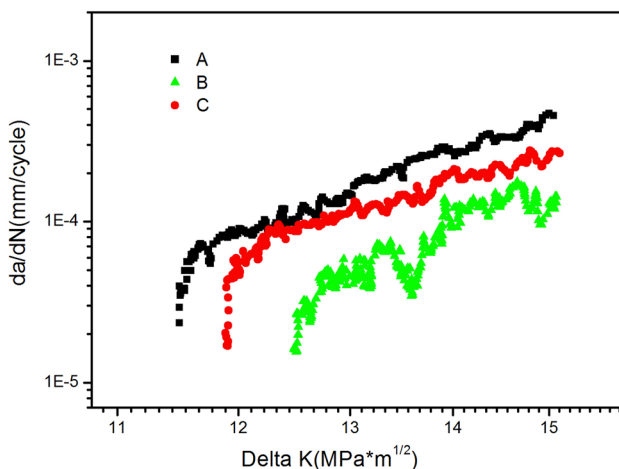


Fig. 2 FCP rates, da/dN as a function of the stress intensity factor range (ΔK) for annealed Al-Cu-Mg alloy

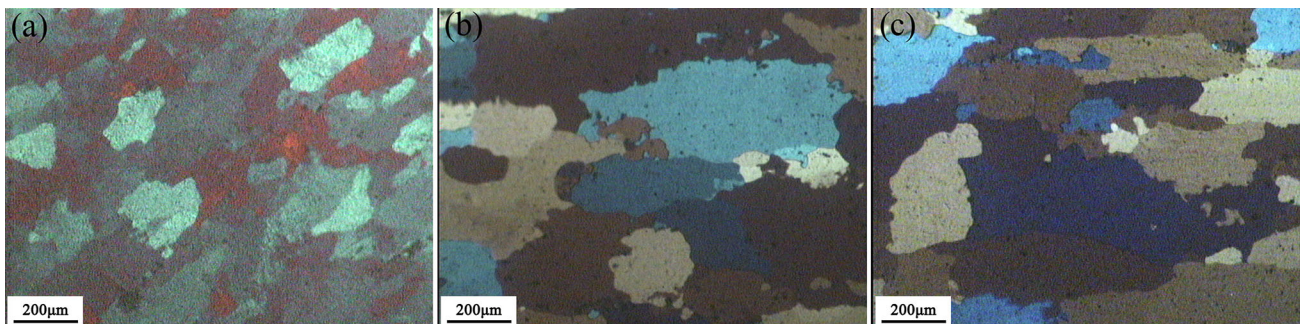


Fig. 3 Optical micrographs illustrating the grain morphology of sample A (a), sample B (b) and sample C (c)

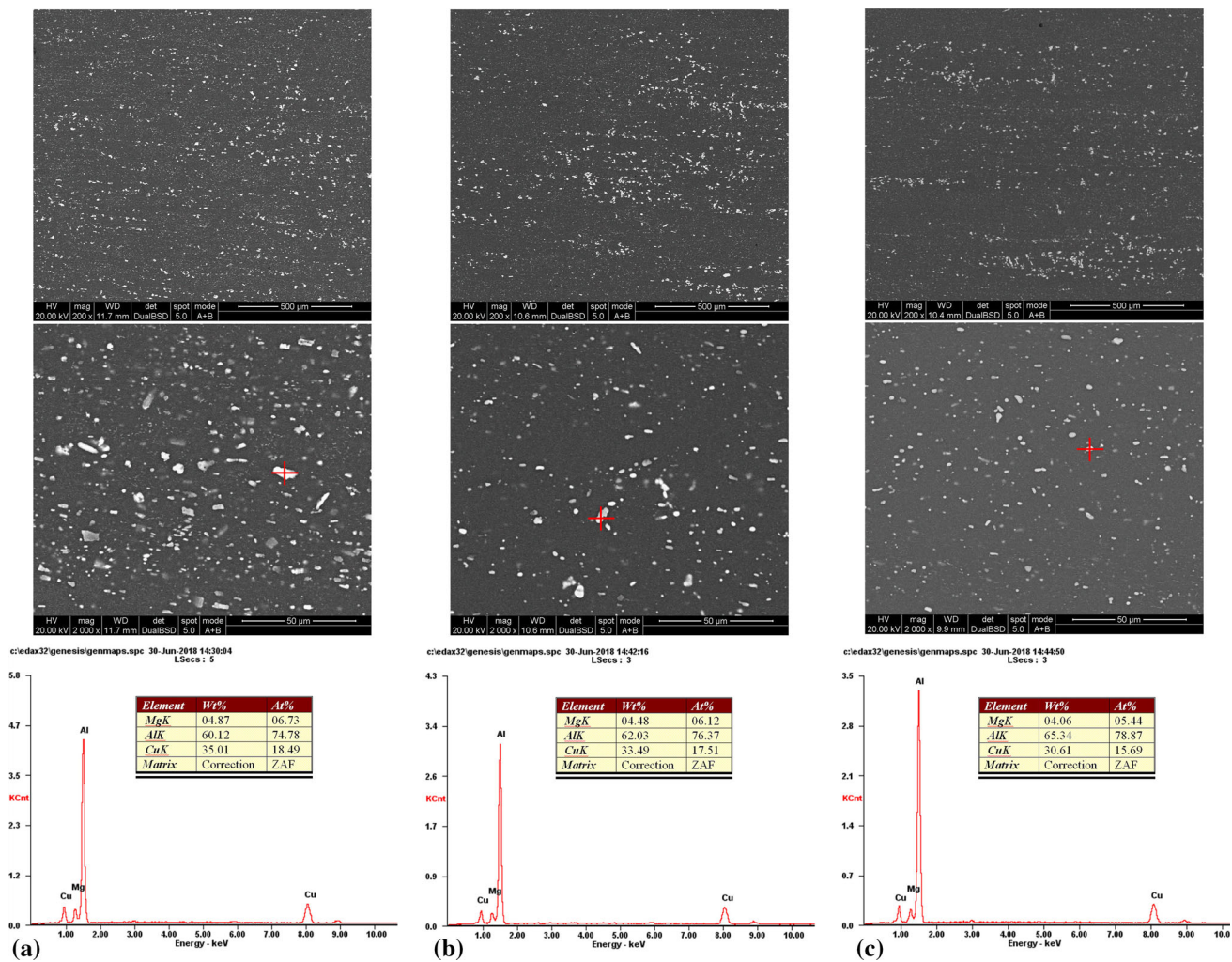


Fig. 4 BSE images and EDS analysis of secondary phases of sample A (a), sample B (b) and sample C (c)

microscopic crack nucleation in the matrix between closely spaced debonded particles (Ref 23) and consequently accelerating the fatigue crack propagation (Ref 26, 30). Therefore, the large and dense secondary particles should be partly responsible for the high FCP rates of sample A. Except for the coarse secondary particles, some fine and dispersive T precipitates were also observed in all annealed samples, as shown in Fig. 5. T particles were regarded as the effective barriers to dislocation slip (Ref 31). However, no significant difference in the number density of T particles among various annealed samples indicates that the effect of T particles on the FCP rate can be ignored.

4.2 Grain Structures and PSBs

The optical micrographs in Fig. 3 showed that the grains in the Brass-textured sample A were smaller than the other textured samples. TEM observation in Fig. 5 revealed that a plenty of subgrains formed in grain interior in sample A. It has been revealed that the small grain size is harmful for enhancing the fatigue crack resistance (Ref 26, 32). The reason is that the grain boundary can act as a barrier for the reversible planar slip, consequently restraining the formation of the persistent slip band (PSB) while PSBs were supposed to be beneficial to improve the fatigue resistance performance (Ref 6, 26, 27). On

the one hand, the formation of PSBs intrinsically need a high level reversible planar slip, which is capable of reducing the fatigue damage accumulation. On the other hand, PSBs can promote more crack deflections along favored slip systems, giving rise to a tortuous crack path. This tortuous crack path may contribute to the onset of roughness-induced crack closure (RICC). As shown in Fig. 6, the Brass-textured sample A showed less PSBs and a lower crack closure level as compared to the other two textured samples. This reflected the negative effect of small grains on enhancing FCP resistance to some extent. However, except for grain size, the grain orientation was also able to affect the formation of PSBs. Table 4 represents the Schmid factors of the slip systems $\{111\}\langle 110\rangle$ for the longitudinal loading direction in the grains with the Brass, Goss or Cube orientations. In the calculation of Schmid factors, the direction $[-112]$ was selected as the longitudinal direction of the Brass grain while the $[001]$ direction was selected as the longitudinal direction of the Goss and Cube grains. It can be found that the biggest Schmid factors in Brass, Goss or Cube grains all reached 0.408. However, there were only two slip systems with the largest Schmid factor in the Brass grain. In contrast, as many as eight slip systems with the largest Schmid factor were, respectively, found in the Goss and Cube grains. It suggested that at the same stress level, the number of activated

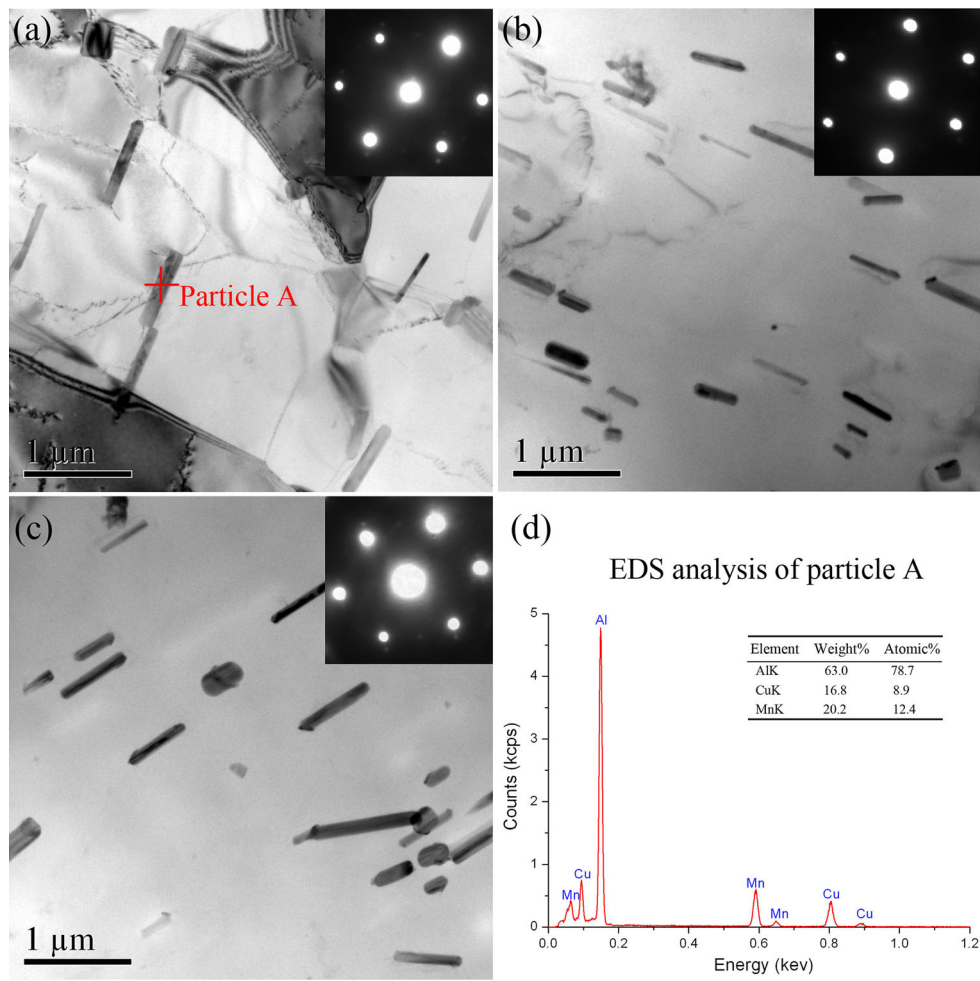


Fig. 5 TEM bright field micrographs and corresponding SAED patterns of sample A (a), sample B (b) and sample C (c)

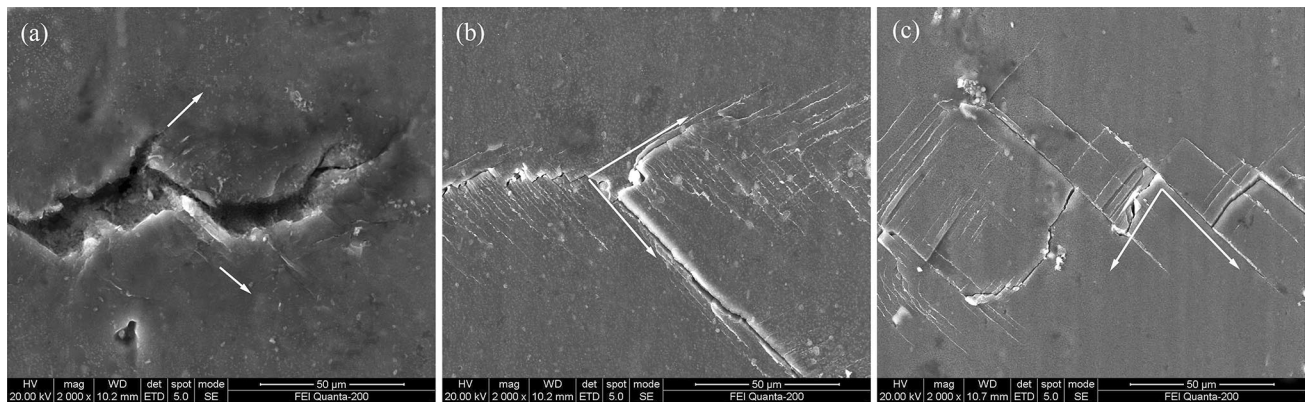


Fig. 6 The surface morphology near the fatigue crack tip of sample A (a), sample B (b) and sample C (c)

slip systems in the Brass grain was much less than that in the Goss or Cube grain. As a result, less PSBs induced by the limited activated slip formed in the surface of Brass grains. Oppositely, more activated slip in Goss and Cube grains brought about more PSBs developing along different directions, promoting more crack deflections, and consequently led to more tortuous crack paths. This tortuous crack was responsible for the high levels of RICC, and thereby reduced the FCP rate.

Besides, operating more slip systems indicated that more energy was consumed, externally reducing the fatigue driving force. In contrast, the cycle plastic deformation relying on limited slip systems easily brought about the stress concentration, benefiting the crack nucleation and accelerated crack propagation. Hence, the Brass-textured sheet represented a relatively smaller fatigue threshold value and a high FCP rate than the other textured sheets.

Table 3 The orientations of grains near fatigue crack of samples A, B and C

Samples	Grains	Measured indices	Simplified indices	Measured texture
Sample A	A	(-5 -22 23)[15 -17 -13]	(0 -1 1)[1 -1 -1]	Close to Brass
	B	(2 -19 16)[23 -6 -10]	(0 -1 1)[2 -1 -1]	Close to Brass
	C	(-2 -23 22)[19 -9 -7]	(0 -1 1)[2 -1 -1]	Close to Brass
	D	(-3 -21 22)[19 -9 -6]	(0 -1 1)[2 -1 -1]	Close to Brass
Sample B	A	(1 1 9)[9 0 -1]	(0 0 1)[1 0 0]	Close to Cube
	B	(2 15 10)[20 0 -4]	(0 1 1)[1 0 0]	Close to Goss
	C	(1 1 6)[0 -6 1]	(0 0 1)[0 -1 0]	Close to Cube
	D	(3 13 24)[2 -6 3]	(0 1 2)[1 3 -1]	Close to Goss
	E	(3 5 27)[1 -33 6]	(0 0 1)[0 -1 0]	Close to Cube
	F	(1 4 8)[4 -15 7]	(0 1 2)[1 -5 2]	Close to Goss
	G	(3 4 21)[1 -27 5]	(001)[0 -1 0]	Close to Cube
Sample C	A	(11 -6 22)[-4 -11 5]	(1 -1 2)[-1 -2 1]	Close to Copper
	B	(5 19 18)[-19 -8 11]	(0 1 1)[-2 -1 1]	Close to Brass
	C	(2 0 11)[-33 2 6]	(0 0 1)[-1 0 0]	Close to Cube
	D	(3 1 11)[-11 -22 5]	(0 0 1)[1 -2 0]	Close to r-Cube
	E	(3 5 20)[0 -20 5]	(0 1 4)[0 -4 -1]	Close to Cube
	F	(1 3 9)[9 3 -2]	(0 1 3)[1 0 0]	Close to Cube

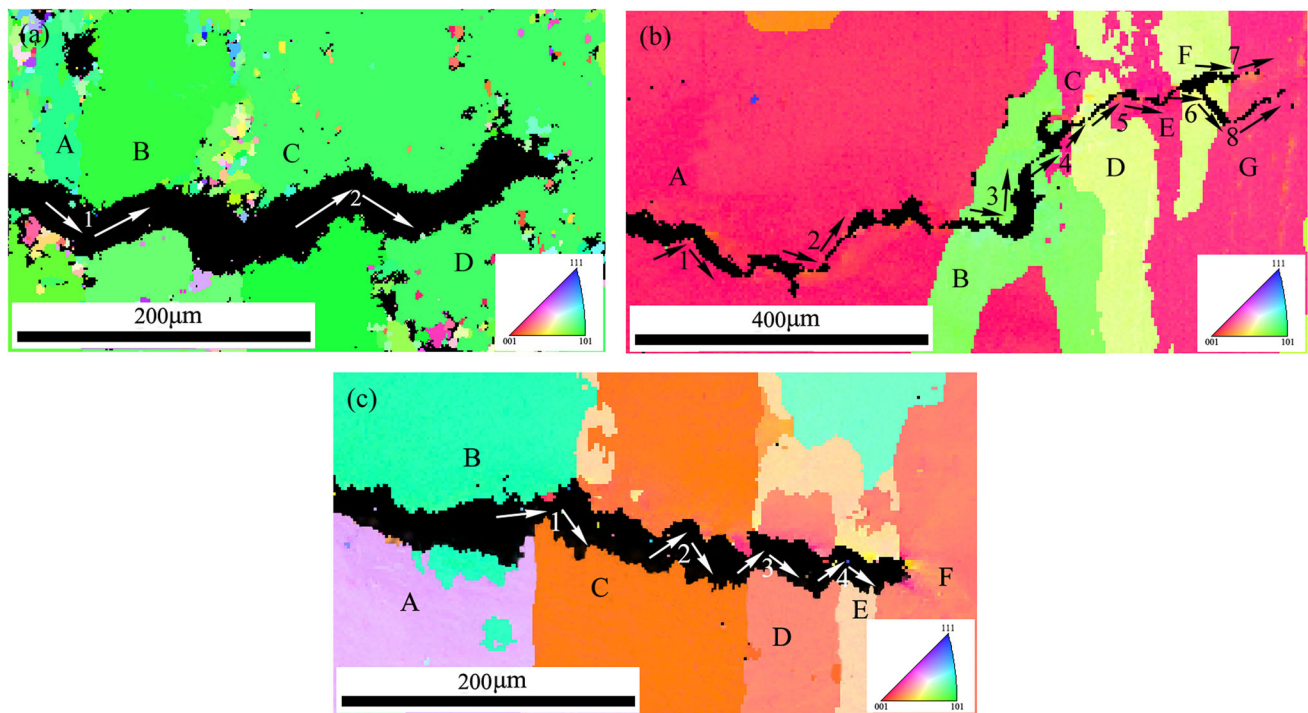


Fig. 7 EBSD observation to the fatigue crack propagation path in sample A (a), sample B (b) and sample C (c)

4.3 Grain Orientation and Crack Deflection

Based on the above, the worse fatigue performance of the Brass-textured sheet A should be attributed to the dominant Brass orientation, numerous large secondary particles and the small grain size. However, the Goss + Cube textured sheet B and the Cube textured sheet C were found to have similar grain sizes and particle distribution but showed no significant difference in FCP rates. More important, Goss grains and Cube grains have the same number of high Schmid factor slip systems, as shown in Table 4. This suggests that the

there should be other reasons giving rise to the fatigue performance difference between samples B and C. Zhai (Ref 16) and Liu (Ref 17) have found that Goss grains could induce large crack deflections, and consequently offer high resistance to the crack propagation across their boundaries. In view of numerous dramatic crack deflections occurring in Goss + Cube textured sheet, as shown in Fig. 7(b), it can be implied that the crack deflection determined by the grain orientation may be the main factor causing the different fatigue performances.

Table 4 Schmid factors of the slip system $\{111\}\langle 110 \rangle$ for the grains with the Brass, Goss or Cube orientations in the longitudinal loading direction

Slip systems	<i>m</i> for Brass	<i>m</i> for Goss	<i>m</i> for Cube
(111) $[\bar{1}\bar{1}0]$	0.272	0	0
(111) $[0\bar{1}1]$	0.136	0.408	0.408
(111) $[\bar{1}01]$	0.408	0.408	0.408
$(\bar{1}\bar{1}1)[101]$	0.272	0.408	0.408
$(\bar{1}\bar{1}1)[110]$	0	0	0
$(\bar{1}\bar{1}1)[0\bar{1}1]$	0.272	0.408	0.408
$(\bar{1}\bar{1}1)[110]$	0	0	0
$(\bar{1}\bar{1}1)[011]$	0	0.408	0.408
$(\bar{1}\bar{1}1)[\bar{1}01]$	0	0.408	0.408
$(11\bar{1})[\bar{1}\bar{1}0]$	0.272	0	0
$(11\bar{1})[011]$	0.408	0.408	0.408
$(11\bar{1})[101]$	0.136	0.408	0.408

Zhai (Ref 15) proposed that the crack deflection at the grain boundary could be characterized by the two angles: the twist angle α and the tilt angle β , which can be expressed as follows:

$$\alpha = \arccos([E] \times [N_1] \cdot [E] \times [N_2]) \quad (\text{Eq 1})$$

$$\beta = \arccos([Z] \times [N_1] \cdot [Z] \times [N_2]) \quad (\text{Eq 2})$$

where $[E]$, $[Z]$, $[N_1]$ and $[N_2]$ are the unit vectors of the grain boundary plane normal, sample surface normal and the normal of the two favored slip planes in the neighboring grains, respectively, in the sample coordinate system. The crystallographic mechanism for the crack deflection can be expressed by the model shown in Fig. 8. The orientation of a slip plane is defined by the two angles θ and φ . θ is the angle between the load axis and the surface trace of the slip plane and φ is the angle between the load axis and the intersection line of the slip plane and the grain boundary plane. The twist angle $\alpha = |\varphi_2 - \varphi_1|$ while the tilt angle $\beta = |\theta_2 - \theta_1|$. It was reported that the large α indicated a high resistance for the crack propagating across the grain boundary (Ref 15). The reason is that the wedge-shaped area (ΔABC in Fig. 5) has to be fractured when the crack propagates from one slip plane to the another slip plane. A large α means a large wedge-shaped area, resulting in high energy consumption during the fatigue crack propagating across this large wedge-shaped area. Thereby the grain boundary with a large α can provide a high resistance for crack growth.

The grain orientation indices of $(hkl)[uvw]$ in the crystal coordinate system were acquired by EBSD as shown in Table 3. However, this orientation defined in the crystal coordinate system should undergo a convert by a 3×3 transformation matrix \mathbf{B} to accommodate the sample coordinate system (L–T–S coordinate system). \mathbf{B} is given by

$$\mathbf{B} = \begin{bmatrix} a_{11} & a_{12} & a_{13} \\ a_{21} & a_{22} & a_{23} \\ a_{31} & a_{32} & a_{33} \end{bmatrix}$$

where each row of the elements in \mathbf{B} are the direction cosines of one of the $[100]$, $[010]$ and $[001]$ axes with L, T and S separately. The vector $[hkl]$ in the crystal coordinate system is normal to the sample surface, and the vector $[uvw]$ in the crystal coordinate system is parallel to the longitudinal direction of the sample. Therefore, they are parallel to S axis and L axis, respectively, in sample coordinate system and the direction of T axis was parallel to the vector $[hkl] \times [uvw]$.

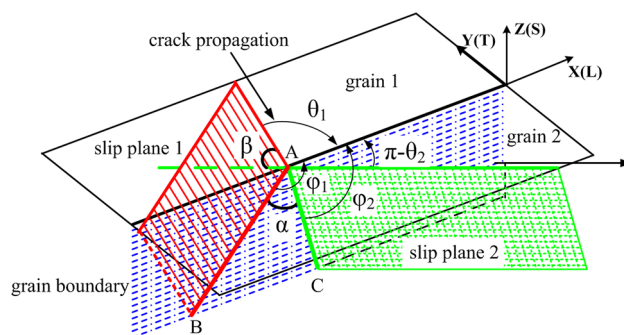


Fig. 8 Schematic diagram showing a crystallographic mechanism for short crack propagation from grain 1 to grain 2

By means of \mathbf{B} , the normal direction of all the possible slip plane can be calculated in the sample coordinate system with the relationship $[N] = [n] \cdot \mathbf{B}$, where $[N]$ and $[n]$ are the unit row vectors of the normal of a slip plane in the sample and crystal coordinate systems, respectively. Assuming that the GB plane is parallel to the load axis (L axis), and perpendicular to the sample surface (L–T plane), the angles θ and φ can be calculated by the equations:

$$\theta = \arccos([N] \times [S] \cdot [L]) \quad (\text{Eq 3})$$

$$\phi = \arccos([N] \times [T] \cdot [L]) \quad (\text{Eq 4})$$

The θ angles corresponding with all possible slip planes can be calculated using Eq 3. Comparing these calculated θ angles with the observed θ angle, the actual operative slip plane can be identified. And then the φ angle for this actual operative slip plane can be obtained by Eq 4. Through calculating the angles θ and φ of the neighboring grains, the calculated twist angle α and tilt angle β for the actual crack deflection at the grain boundary can be acquired. Besides crack deflections at grain boundary, a fair amount of large crack deflections in grains interior were observed, as shown in Fig. 7. These crack deflections in grains interior were mainly induced by the hindering effect of secondary particles on the slip. During the cycle deformation, the dislocations could continuously pile up in the large secondary particles, resulting in the local stress concentration on the particles and finally inducing the activation of a new slip system. As a result, crack deflections often occur when the fatigue crack propagated across the large

Table 5 Calculated twist or tilt angles for the crack deflections in annealed Al-Cu-Mg alloy

Samples	Crack deflections	Related grains	Crack/slip planes	Twist angles α ,°	Tilt angles β ,°
A	1	A and B	($\bar{1}11$) and ($1\bar{1}1$)	20.1	69.9
	2	C and D	($\bar{1}\bar{1}1$) and (111)	25.2	76.1
B	1	A and A	($\bar{1}11$) and ($11\bar{1}$)	11.5	92.0
	2	A and A	(111) and ($1\bar{1}\bar{1}$)	10.8	83.3
	3	B and B	($\bar{1}11$) and ($11\bar{1}$)	33.2	109.4
	4	B and C	(111) and ($1\bar{1}\bar{1}$)	53.7	14.6
	5	D and E	($\bar{1}\bar{1}1$) and ($\bar{1}11$)	34.4	53.4
	6	F and F	($\bar{1}\bar{1}1$) and ($\bar{1}11$)	34.1	79.1
	7	F and G	($11\bar{1}$) and ($\bar{1}11$)	82.9	22.3
	8	F and G	(111) and ($1\bar{1}\bar{1}$)	57.4	88.3
C	1	B and C	($1\bar{1}\bar{1}$) and ($1\bar{1}\bar{1}$)	25.6	46.5
	2	C and C	($\bar{1}\bar{1}1$) and (111)	10.5	94.2
	3	C and D	($\bar{1}\bar{1}1$) and (111)	16.6	113.1
	4	D and E	($\bar{1}11$) and ($1\bar{1}\bar{1}$)	13.4	105.3

particles. The α and β angles for some representative crack deflections in grains interior were also calculated. To some extent, this hindering effect of secondary particles on crack propagation is similar to that of grain boundary. However, the former hindering effect should be much weaker than the latter, because the interface between the secondary phase and the matrix was much smaller than the grain boundary. Table 5 represents the calculated α , β angles for the crack deflections in different samples. For sample A, crack deflection 1 at the boundary between grains A and B possessed a twist angle of 20.1°. Crack deflection 2 at the boundary between grains C and D possessed a twist angle of 25.2°. The orientations of grains A, B, C and D were all close to the Brass orientation, as shown in Table 3. For sample B, crack deflections 1 and 2 in the interior of Cube-grain A possessed relatively small twist angles, arriving at 11.5° and 10.8°, respectively. In contrast, crack deflections 3 and 6 in the interior of Goss and near-Goss grains, represented relatively large twist angles, arriving at 33.2° and 34.1°, respectively. The other crack deflections including deflections 4, 5, 7 and 8 at the Goss-Cube grain boundary, also possessed large twist angles as shown in Table 5. For sample C, crack deflection 1 at the grain boundary between Brass-grain B and Cube-grain C showed a medium twist angle of 25.6° and deflection 2 in the interior of Cube-grain C showed a twist angle of 10.5°. Besides, the crack deflections 3 and 4 at grain boundary of near-Cube grains showed the small twist angles of 16.6° and 13.4°, respectively. Based on the above, it can be found that Goss grains could offer larger twist angles to crack deflections than Brass grains. This was consistent with the previous discovery revealed by Zhai (Ref 16), showing that the Goss grain was more likely to provide large twist angles for its neighboring grains than the Brass grain. For Cube grains, large twist angles were offered to the crack deflections at the Cube-Goss grain boundary while small twist angles were offered to the crack deflections in Cube grains interior or at the grain boundary between two near-Cube grains. In contrast, Goss grains could offer large twist angles to the crack deflections either in grains interior or at grain boundary. In other words, Goss grains could more easily induce crack deflections with large twist angles as compared to Cube grains. As mentioned above, the crack deflection with a large twist angle was in favor of improving FCP resistance. Thereby more Goss grains could induce more this kind of crack deflections, undoubtedly leading to a higher FCP resistance. Hence it is

well understood that the Goss + Cube textured sample B showed the lower FCP rate than the Cube textured sample C. In addition, the crack branch near crack deflection 4 was found at the Goss-Cube grain boundary shown in Fig. 7(b). This crack branch was mainly caused by the high-resistant Goss-Cube grain boundary with a high twist angle. Because when the crack reached the high-resistant Goss-Cube grain boundary, the crack may propagate along the new slip plane, thereby leading to the crack branch developing. This crack branch as a secondary crack was considered to be in favor of reducing the fatigue crack driving force and thereby enhancing the FCP resistance (Ref 23, 25, 26). Besides, it was found that the fatigue crack showed the ability of selecting a favorable path to propagate across the grain boundary. When the crack propagated across the Goss-Cube grain boundary in sample B, as shown in Fig. 7(b), crack deflection 7 in sample B showed a twist angle of 82.9°, while crack deflection 8 showed a relatively smaller twist angle of 57.4°. As a result, the crack was more easily propagate across the high-resistant Goss-Cube grain boundary through the crack deflection 8 while the crack branch containing crack deflection 7 was retarded. In near-threshold regime, due to the low level of cycle stress, the newborn fatigue crack was likely to be retarded when it propagated to these high-resistant grain boundaries. Therefore, the Goss + Cube textured sheet with more high-resistant grain boundaries represented a higher fatigue threshold value and a lower FCP rate in near -threshold regime than the Cube textured sheet.

5. Conclusions

- (1) The Goss + Cube textured sheet possessed the lowest FCP rate and the largest fatigue threshold value, while the Brass-textured sheet possessed the highest FCP rate and the smallest fatigue threshold value.
- (2) The worst fatigue performance of the Brass-textured sheet is a consequence of the combined effect of the small grain size, the dense secondary particles distribution and the dominant Brass texture.
- (3) Goss and Cube grains, have more high Schmid factor slip systems than Brass grains, promoting PSBs formation and externally applied energy consumption, finally giving rise to a high resistance to FCP.

- Goss grains could induce crack deflection with large twist angles, resulting in more energy consumption during the cracking process and thereby enhance the FCP resistance.

Acknowledgments

The authors are grateful for financial support from the National Key Research and development Program of China (Grant No. 2016YFB0300900), the National Key Fundamental Research Project of China (2012CB619506-3), National Natural Science Foundation of China (51171209), and 2011 Program of Ministry of Education of China.

References

- T.S. Srivatsan, D. Kolar, and P. Magnusen, The Cyclic Fatigue and Final Fracture Behavior of Aluminum Alloy 2524, *Mater. Sci. Eng. A*, 2001, **314**, p 118–130
- J.C. Williams and E.A. Starke, Progress in Structural Materials for Aerospace Systems, *Acta Mater.*, 2003, **51**, p 5775–5799
- J.X. Li, T. Zhai, M.D. Garratt, and G.H. Bray, Four-Point-Bend Fatigue of AA 2026 Aluminum Alloys, *Metall. Mater. Trans. A*, 2005, **36**, p 2529–2539
- S.P. Ringer, T. Sakurai, and I.J. Polmear, Origins of Hardening in Aged Al-Cu-Mg-(Ag) Alloys, *Acta Mater.*, 1997, **45**, p 3731–3744
- G.H. Bray, M. Glazov, R.J. Rioja, D. Li, and R.P. Gangloff, Effect of Artificial Aging on the Fatigue Crack Propagation Resistance of 2000 Series Aluminum Alloys, *Int. J. Fatigue*, 2001, **23**, p 265–276
- N. Kamp, N. Gao, M.J. Starink, and I. Sinclair, Influence of Grain Structure and Slip Planarity on Fatigue Crack Growth in Low Alloying Artificially Aged 2xxx Aluminium Alloys, *Int. J. Fatigue*, 2007, **29**, p 869–878
- W.L. Morris, Microcrack Closure Phenomena for Al, 2219-T851, *Metall. Mater. Trans. A*, 1979, **10**(1), p 5–11
- Y. Xue, H.E. Kadir, M.F. Horstemeyer, J.B. Jordon, and H. Weiland, Micromechanisms of Multistage Fatigue Crack Growth in a High-Strength Aluminum Alloy, *Acta Mater.*, 2007, **55**, p 1975–1984
- Z.Q. Zheng, B. Cai, T. Zhai, and S.C. Li, The Behavior of Fatigue Crack Initiation and Propagation in AA2524-T34 alloy, *Mater. Sci. Eng. A*, 2011, **528**, p 2017–2022
- M. Liu, Z.Y. Liu, S. Bai, P. Xia, P. Ying, and A. Wang, Analysis on the Dissolution Behavior of Various Size Cu-Mg Coclusters Near a Fatigue Crack Tip of Underaged Al-Cu-Mg Alloy During Cyclic Loading, *J. Alloys Compd.*, 2017, **699**, p 119–125
- M. Liu, Z.Y. Liu, S. Bai, P. Xia, P. Ying, and S. Zeng, Solute Cluster Size Effect on the Fatigue Crack Propagation Resistance of an Underaged Al-Cu-Mg Alloy, *Int. J. Fatigue*, 2016, **84**, p 104–112
- Y.Q. Chen, S.P. Pan, M.Z. Zhou, D.Q. Yi, D.Z. Xu, and Y.F. Xu, Effects of Inclusions, Grain Boundaries and Grain Orientations on the Fatigue Crack Initiation and Propagation Behavior of 2524-T3 Al Alloy, *Mater. Sci. Eng. A*, 2013, **580**, p 150–158
- K. Hockauf, F.X. Wagner, T. Halle, T. Niendorf, M. Hockauf, and T. Lampke, Influence of Precipitates on Low-Cycle Fatigue and Crack Growth Behavior in an Ultrafine-Grained Aluminum Alloy, *Acta Mater.*, 2014, **80**, p 250–263
- Aladar A. Csontos and E.A. Starke, The Effect of Inhomogeneous Plastic Deformation on the Ductility and Fracture Behavior of Age Hardenable Aluminum Alloys, *Int. J. Plast.*, 2005, **21**(6), p 1097–1118
- T. Zhai, A.J. Wilkinson, and J.W. Martin, A Crystallographic Mechanism for Fatigue Crack Propagation Through Grain Boundaries, *Acta Mater.*, 2000, **48**, p 4917–4927
- T. Zhai, X.P. Jiang, J.X. Li, M.D. Garratt, and G.H. Bray, The Grain Boundary Geometry for Optimum Resistance to Growth of Short Fatigue Cracks in High Strength Al-Alloys, *Int. J. Fatigue*, 2005, **27**, p 1202–1209
- Z.Y. Liu, F.D. Li, P. Xia, S. Bai, and Y.X. Gu, D. Y, and S.M. Zeng, Mechanisms for Goss-Grains Induced Crack Deflection and Enhanced Fatigue Crack Propagation Resistance in Fatigue Stage II, of an AA2524 Alloy, *Mater. Sci. Eng. A*, 2015, **625**, p 271–277
- F.D. Li, Z.Y. Liu, W. Wu, P. Xia, P.Y. Ying, Q. Zhao, J.L. Li, S. Bai, and C.W. Ye, On the Role of Texture in Governing Fatigue Crack Propagation Behavior of 2524 Aluminum Alloy, *Mater. Sci. Eng. A*, 2016, **669**, p 367–378
- W.T. Wu, Z.Y. Liu, Y.C. Hu, F.D. Li, S. Bai, P. Xia, A. Wang, and C.W. Ye, Goss Texture Intensity Effect on Fatigue Crack Propagation Resistance in an Al-Cu-Mg Alloy, *J. Alloys Compd.*, 2018, **730**, p 318–326
- P.S. Bate, Y. Huang, and F.J. Humphreys, Development of the “Brass” Texture Component During the Hot Deformation of Al-6Cu-0.4Zr, *Acta Mater.*, 2004, **52**, p 4281–4289
- Q. Zhao, Z.Y. Liu, T.T. Huang, P. Xia, and F.D. Li, Enhanced Fracture Toughness in an Annealed Al-Cu-Mg Alloy by Increasing Goss/Brass Texture Ratio, *Mater. Charact.*, 2016, **119**, p 47–54
- S.C. Wang and M.J. Starink, Precipitates and intermetallic phases in precipitation hardening Al-Cu-Mg-(Li) based alloys, *Int. Mater. Rev.*, 2005, **50**, p 193–215
- Y.Q. Chen, D.Q. Yi, Y. Jiang, B. Wang, D.Z. Xu, and S.C. Li, Twinning and Orientation Relationships of T-phase Precipitates in an Al Matrix, *J. Mater. Sci.*, 2013, **48**, p 3225–3231
- Q. Zhao, Z.Y. Liu, S.S. Li, Y.C. Hu, and S. Bai, Effect of S Phase Characteristics on the Formation of Recrystallization Textures of an Al-Cu-Mg Alloy, *J. Alloys Compd.*, 2018, **747**, p 293–305
- B. Künkler, O. Düber, P. Köster, U. Krupp, C.P. Fritzen, and H.J. Christ, Modelling of Short Crack Propagation—Transition from Stage I, to Stage II, *Eng. Fract. Mech.*, 2008, **75**, p 715–725
- S. Bai, Z.Y. Liu, Y.T. Li, Y.H. Hou, and X. Chen, Microstructures and Fatigue Fracture Behavior of an Al-Cu-Mg-Ag Alloy with Addition of Rare Earth Er, *Mater. Sci. Eng. A*, 2010, **527**(7–8), p 1806–1814
- S. Suresh, A.K. Vasudevan, and P.E. Bretz, Mechanisms of Slow Fatigue Crack-Growth in High-Strength Aluminum Alloys: Role of Microstructure and Environment, *Metall. Trans. A*, 1984, **15**, p 369–379
- J. Man, T. Vystavěl, A. Weidner, I. Kuběna, M. Petreenc, and T. Kruml, Study of Cyclic Strain Localization and Fatigue Crack Initiation Using FIB Technique, *Int. J. Fatigue*, 2012, **39**, p 44–53
- L.L. Wei, Q.L. Pan, H.F. Huang, L. Fei, and Y.L. Wang, Influence of Grain Structure and Crystallographic Orientation on Fatigue Crack Propagation Behavior of 7050 Alloy Thick Plate, *Int. J. Fatigue*, 2014, **66**(9), p 55–64
- P. Xia, Z.Y. Liu, S. Bai, L.Q. Lu, and L.F. Gao, Enhanced Fatigue Crack Propagation Resistance in a Superhigh Strength Al-Zn-Mg-Cu Alloy by Modifying RRA Treatment, *Mater. Charact.*, 2016, **118**, p 438–445
- G.J. Mahon, J.M. Howe, and A.K. Vasudevan, Microstructural Development and the Effect of Interfacial Precipitation on the Tensile Properties of an Aluminum, Silicon-Carbide Composite, *Acta Metal. Mater.*, 1990, **38**, p 1503–1512
- N. Kamp, N. Gao, M.J. Starink, and I. Sinclair, Influence of Grain Structure and Slip Planarity on Fatigue Crack Growth in Low Alloying Artificially Aged 2xxx Aluminium Alloys, *Int. J. Fatigue*, 2007, **29**, p 869–878